Computations of Supersonic Flow over a Missile Afterbody Containing an Exhaust Jet

Jubaraj Sahu*
U.S. Army Ballistic Research Laboratory, Aberdeen Proving Ground, Maryland

A thin-layer compressible Navier-Stokes code, developed for projectile aerodynamics, has been used to compute the supersonic flow over a missile afterbody containing a centered exhaust jet and the equations are solved using a time-dependent, implicit numerical algorithm. A unique flowfield segmentation procedure is used that preserves the sharp base corner and facilitates the adaption of the grid to the free shear layer in the base region. Solutions have been obtained for an axisymmetric, boattailed afterbody where the freestream Mach number is 2.0 and the jet exit Mach number is 2.5. Computations were made at various jet static pressure to freestream static pressure ratios of 1-9. Qualitative features of the base region flowfield seen experimentally are very well observed in the computed results. Quantitative comparisons of base pressure with the experiment indicate good agreement at high pressure ratios and some disagreement at low pressure ratios.

Introduction

THE flowfield in the base region of a jet-propelled tactical missile or a rocket-assisted artillery projectile is complex. The propulsive jet is underexpanded and can strongly affect the base pressure distribution and the afterbody flowfield. For large jet to freestream pressure ratios, the interaction of the exhaust jet with the external flow can be large enough to induce extensive afterbody flow separation. This can, of course, seriously affect the control effectiveness of any control surface located in that region. For over a decade, experimental efforts and the component approach of Korst[1] have provided valuable insight into this flow problem. The flowfield under consideration is complicated due to strong viscous/inviscid interaction and regions of flow separation. The component approach has its serious limitations for three-dimensional configurations and similar procedures are extremely difficult to apply at transonic speeds.[2]

Recent advances in numerical algorithms and the advent of supercomputers have made numerical modeling of the Navier-Stokes equations a reality. As computational speed has sharply increased, the computing costs have sharply dropped. This trend in technology makes the direct solution of Navier-Stokes equations even more attractive. The Navier-Stokes computational technique models the strong interactions involved between the flow regimes in a fully coupled manner and does not contain the empiricism found in the component approach. Some empiricism does enter into the Navier-Stokes solutions through turbulence modeling, which is an area of further computational and experimental research.

Recently, Sahu et al.[3] computed the base region flowfield for a projectile at transonic speeds using the thin-layer Navier-Stokes equations. A unique flowfield segmentation procedure was used for the complete numerical simulation of a projectile including the base region. This technique was also used to calculate the effect of a centered jet on the base region flowfield at a high transonic speed.[4] Other Navier-Stokes solutions have been obtained for flow over afterbodies with exhaust jet.[5-8] The work of Deiwert[5] and Fox[6] are based on the thin-layer approximation of the Navier-Stokes equations, whereas Wagner[7] and Thomas et al.[8] solved the full Navier-Stokes equations. The two-layer, algebraic, Baldwin-Lomax[9] turbulence model was used in Refs. 3-7. Thomas et al.[8] used the two-equation k-ϵ and k-w turbulence models and some differences in the computed results were observed.

This article describes the computational investigation of the effect of exhaust jet on the base pressure and the base region flowfield at supersonic speed using the same numerical procedure of Refs. 3 and 4. An unique flowfield segmentation procedure, equivalent to using multiple adjoining grids, is used to preserve the sharp base corner. Additionally, the grids in the base region were adapted to the free shear layer as the solutions developed. Solutions have been obtained for supersonic flow over an axisymmetric boattail afterbody where the freestream Mach number is 2.0 and the jet-exit Mach number is 2.5. Ratios of jet static pressure to freestream static pressure are considered in the range of 1-9 for a conical nozzle exit half-angle of 20 deg. Comparison of the numerical results have been made with available experimental data.

Computational Technique

The azimuthal in variant (or generalized axisymmetric) thin-layer Navier-Stokes equations for general spatial coordinates, ζ, η, ξ can be written as[10]

$$\partial_\tau \hat{q} + \partial_\xi \hat{E} + \partial_\zeta \hat{G} + \hat{H} = R^{-1} \partial_\zeta \hat{S} \tag{1}$$

where $\xi = \xi(x,y,z,t)$ is the longitudinal coordinate, $\eta = \eta(y,z,t)$ the circumferential coordinate, $\zeta = \zeta(x,y,z,t)$ the near normal coordinate, $\tau = t$ the time, and

$$\hat{q} = J^{-1} \begin{bmatrix} \rho \\ \rho u \\ \rho v \\ \rho w \\ e \end{bmatrix}, \quad \hat{E} = J^{-1} \begin{bmatrix} \rho U \\ \rho u U + \xi_x p \\ \rho v U + \xi_y p \\ \rho w U + \xi_z p \\ (e+p)U - \xi_t p \end{bmatrix}$$

Received July 22, 1985; presented as Paper 85-1815 at the AIAA Atmospheric Flight Mechanics Conference, Snowmass, CO, Aug. 19-21, 1985; revision received Sept. 22, 1986. This paper is declared a work of the U.S. Government and therefore is in the public domain.

*Aerospace Engineer, Launch and Flight Division. Member AIAA.

$$\hat{G}=J^{-1}\begin{bmatrix}\rho W\\ \rho uW+\zeta_x p\\ \rho vW+\zeta_y p\\ \rho wW+\zeta_z p\\ (e+p)W-\zeta_t p\end{bmatrix}$$

$$\hat{H}=J^{-1}\begin{bmatrix}0\\ 0\\ \rho V[R_\xi(U-\xi_t)+R_\zeta(W-\zeta_t)]\\ -\rho VR(V-\eta_t)-p/R\\ 0\end{bmatrix}$$

$$\hat{S}=\begin{bmatrix}0\\ \mu(\zeta_x^2+\zeta_y^2+\zeta_z^2)u_\zeta+(\mu/3)(\zeta_x u_\zeta+\zeta_y v_\zeta+\zeta_z w_\zeta)\zeta_x\\ \mu(\zeta_x^2+\zeta_y^2+\zeta_z^2)v_\zeta+(\mu/3)(\zeta_x u_\zeta+\zeta_y v_\zeta+\zeta_z w_\zeta)\zeta_y\\ \mu(\zeta_x^2+\zeta_y^2+\zeta_z^2)w\zeta+(\mu/3)(\zeta_x u_\zeta+\zeta_y v_\zeta+\zeta_z w_\zeta)\zeta_z\\ \{(\zeta_x^2+\zeta_y^2+\zeta_z^2)[(\mu/2)(u^2+v^2+w^2)_\zeta\\ +\kappa Pr^{-1}(\gamma-1)^{-1}(a^2)_\zeta]+(\mu/3)\\ (\zeta_x u+\zeta_y v+\zeta_z w)(\zeta_x u_\zeta+\zeta_y v_\zeta+\zeta_z w_\zeta)\}\end{bmatrix}$$

The velocities

$$U=\xi_t+\xi_x u+\xi_y v+\xi_z w$$

$$V=\eta_t+\eta_x u+\eta_y v+\eta_z w$$

$$W=\zeta_t+\zeta_x u+\zeta_y v+\zeta_z w$$

represent the contravariant velocity components.

The Cartesian velocity component (u,v,w) are nondimensionalized with respect to a_∞ (freestream speed of sound). The density ρ is referenced to ρ_∞ and total energy e to $\rho_\infty a_\infty^2$. The local pressure is determined using the equation of state

$$p=(\gamma-1)[e-0.5\rho(u^2+v^2+w^w)] \tag{3}$$

where γ is the ratio of specific heats.

In Eq. (1), axisymmetric flow assumptions have been made that result in the source term $\hat{H}$. The details of how this is obtained can be found in Ref. 10 and are not discussed here. Equation (1) contains only two spatial derivatives. However, it retains all three momentum equations and allows a degree of generality over the standard axisymmetric equations. In particular, the circumferential velocity is not assumed to be zero, thus allowing computations for spinning projectiles to be accomplished.

The numerical algorithm used is the Beam-Warming fully implicit, approximately factored finite-difference scheme. The algorithm can be first- or second-order accurate in time and second- or fourth-order accurate in space. Since the interest is only in the steady-state solution, Eq. (1) is solved in a time-asymptotic fashion and first-order accurate time differencing is used. The spatial accuracy is fourth order. Details of the algorithm are included in Refs. 11–13.

For the computation of turbulent flows, a turbulence model must be supplied. In the present calculations, a two-layer algebraic eddy viscosity model by Baldwin and Lomax[9] is used. In their two-layer model, the inner region follows the Prandtl-Van Driest formulation. Their outer formulation can be used in wakes as well as in attached and separated boundary layers. In both the inner and outer formulations, the distribution of vorticity is used to determine length scales, thereby avoiding the necessity of finding the outer edge of the boundary layer (or wake). The magnitude of the local vorticity for the axisymmetric formulation is given by

$$|\omega|=\sqrt{\left(\frac{\partial u}{\partial x}\right)^2+\left(\frac{\partial v}{\partial z}-\frac{\partial w}{\partial y}\right)^2+\left(\frac{\partial w}{\partial x}-\frac{\partial u}{\partial z}\right)^2} \tag{4}$$

In determining the outer length scale, a function[9]

$$F(y)=y|\omega|[1-\exp(-y^+/A^+)] \tag{5}$$

is used where y^+ and A^+ are the conventional boundary-layer terms. For the base flow (or wake flow), the exponential term of Eq. (5) is set equal to zero, beginning at the first point downstream of the base. In other words, the Van Driest damping term is not applicable and is thus neglected. The outer formulation also requires the computation of the Klebanoff intermittency function and a velocity scale U_{dif} given by

$$U_{\text{dif}}=(u^2+v^2+w^2)^{\frac{1}{2}}_{\max}-(u^2+v^2+w^2)^{\frac{1}{2}}_{\min} \tag{6}$$

Both of the terms on the right-hand side of Eq. (6) are evaluated via the velocity profiles. For wall-bounded flows, the minimum term in U_{dif} is usually zero. For wakes, the Klebanoff intermittency factor is determined by measuring the distance from the centerline of symmetry. The algebraic eddy viscosity model may not be strictly valid for all of the wake flow situations. More realistic or complex turbulence models must be considered a subject left for future study.

Method of Solution

Base Region Flow with Jet Off

The procedure used to compute the base flow without jet for a projectile configuration has been described in Ref. 3; however, limited details will be repeated here for the sake of clarity. The code can compute the full flowfield (including the base region) of a projectile. However, for supersonic flow, the forebody solution can be obtained efficiently using a space-marching parabolized Navier-Stokes (PNS) code. This technique is used to provide the upstream boundary condition (line EF, Fig. 1) for the computation of the afterbody flowfield containing the base region. The afterbody solution is obtained using the unsteady or time-marching Navier-Stokes equations. Figure 1 shows a schematic illustration of the flowfield segmentation used in this study for computational purposes. It illustrates the transformation of the physical domain into the computational domain and the details of the flowfield segmentation procedure in both domains. This flowfield segmentation procedure is equivalent to using multiple adjoining grids. An important advantage of this procedure lies in the preservation of the sharp corner at the base; it allows easy blending of the computational meshes between the regions ABCD and AEFG. No approximation of the actual sharp corner at the base is made as it is inherent in the current procedure.

In Fig. 1, the cross-hatched region represents the model. The line BC is the base and the region ABCD is the base region or the wake. The line AB is a computational cut through the physical wake region, which acts as a repetitive boundary in the computational domain. Implicit integration is carried out in both ξ and ζ directions. Note the presence of the lines BC (base) and EF in the computational domain. They both act as boundaries in the computational domain and special care must be taken in inverting the block tridiagonal matrix in the ξ direction. The details of this procedure can be found in Ref. 3 and are not included here.

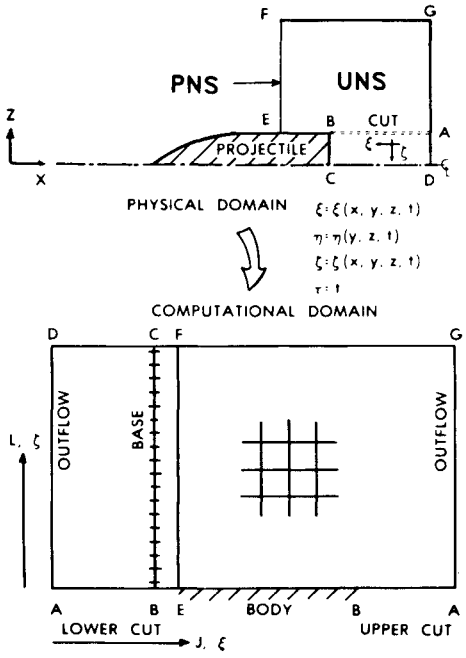

Fig. 1 Schematic illustration of flowfield segmentation.

The no-slip boundary condition for viscous flow is enforced by setting

$$U = V = W = 0 \tag{7}$$

on the body surface including the base. Along the computational cut (AB), the flow variables above and below the cut are simply averaged to determine the boundary conditions on the cut. On the centerline of the wake region, a symmetry condition is imposed and freestream conditions are used on the outer boundary.

Base Region Flow with Jet On

The method of solution for the case with a centered propulsive jet remains essentially the same as described in the previous subsection. The boundary conditions on the body surface, at the cut, and at the downstream boundary also remain the same as previously described. Along the base boundary, the same conditions described earlier are used. For the nozzle exit, boundary conditions are used based on the nozzle exit Mach number, stagnation temperature, and pressure. The velocity components are linearly interpolated from the center line of symmetry to the nozzle height at the exit, i.e., conical flow at the jet exit has been assumed.

Model and Computational Grid

The model geometry used in this study is comprised of a 2 caliber 14 deg half-angle conical nose, a 6 caliber cylindrical midsection, and a 1 caliber 8 deg boattail. The nozzle exit diameter is 0.6 caliber. Detailed experimental measurements for this shape and the same flow conditions described earlier have been made by Agrell and White.[14]

When computations over the entire model are made, only a limited number of grid points can be used in the base region. One way to eliminate this restriction is to use known data given by experiment or otherwise at a station upstream of the base and then compute the flowfield in the isolated base region only. This, of course, allows a large number of grid points to be used in the base region and can be used to determine grid dependency on the computed solution in the base region. This is ideally suited for the numerical computations of base region flowfield at supersonic velocities. Solutions can be obtained for the forebody with the space-marching PNS code. In the present study, the PNS code was used to generate a solution at a station 1.5 calibers upstream of the base; this solution was then used as an upstream boundary condition for the computation of the base region flowfield by the unsteady base flow code. In Ref. 5, computation was made for the entire missile using a time-dependent code that resulted in a coarse grid in the afterbody and the base region. Adequate grid resolution was, thus, not achieved. In addition, the grid in the base region was not smooth and the actual geometry of the base region of the missile was not modeled accurately. In the present computations, we have used the technique described above that allowed a large number of grid points to be used in the afterbody and base region and adequate grid resolution was achieved. Note that the actual geometry of the missile was accurately modeled.

Figures 2–5 show the expanded view of the computational grids in the base region. These grids are shown for both the upper and lower halves for clarity; however, computations are made only for the upper half-plane for axisymmetric

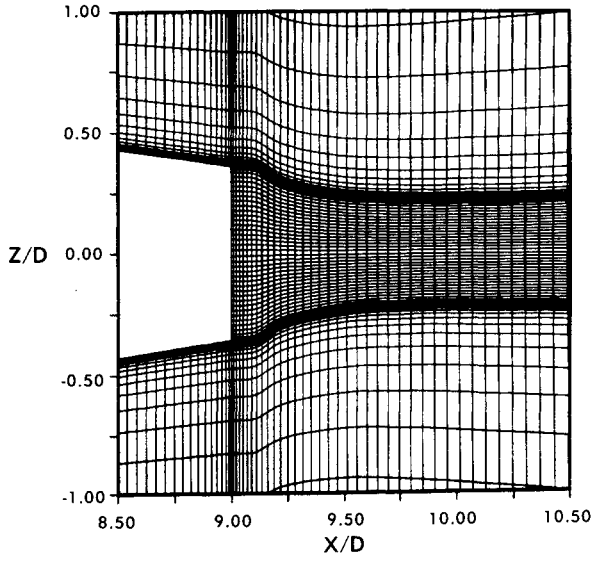

Fig. 2 Computational grid in the base region, jet off.

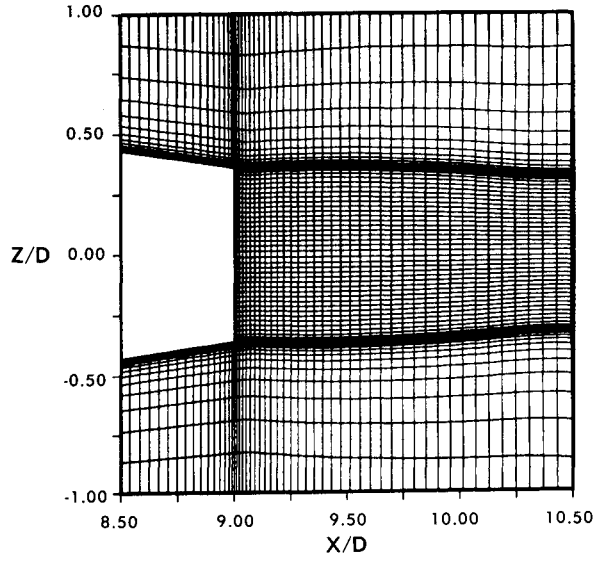

Fig. 3 Computational grid in the base region, jet on, $P_j/P_\infty = 1.0$.

flow. Figure 2 shows the grid for the jet-off case, whereas the grids shown in Figs. 3-5 are for the jet-on cases of $P_j/P_\infty = 1$, 3, and 9, respectively. Additionally, these grids were adapted to the free shear layer as the solutions developed. Logic has been implemented to adjust the grid cut AB (Fig. 1) to the viscous shear layer that begins to neck down shortly behind the base. The height of the cut is weighted between a moment of shear and the standard nonadaptive grids. Specifically, the cut height $\bar{z}$, at each j location, is determined by the relation

$$\bar{z}_j = \frac{\Sigma(\delta_z u_{j\ell})^2 z_{j\ell} + \epsilon D/2}{\Sigma(\delta_z u_{j\ell})^2 + \epsilon} \tag{8}$$

where the ℓ summation is carried out only for those points within an interval $0.2D \le z_{j\ell} \le 2D$. Here, D is the base diameter, δ_z a central difference operator, and ϵ a positive parameter that ensures a standard grid if all $\delta_z u_{j\ell}$ are zero or if ϵ is very large. Additional averaging is used in the x direction (longitudinal direction). Each of these grids consisted of 200 points in the longitudinal direction with 80 points located in the base region and 50 points in the normal direction. This grid size is considered adequate based on the experience gained in trying various grid sizes for a similar problem.[4] The minimum grid spacing used here is $0.00002D$, which corresponds to $y+ \simeq 1$. Details of the grid patching used consistent with the flowfield segmentation procedure and the strategy of clustering of grid points can be found in Refs. 3 and 4.

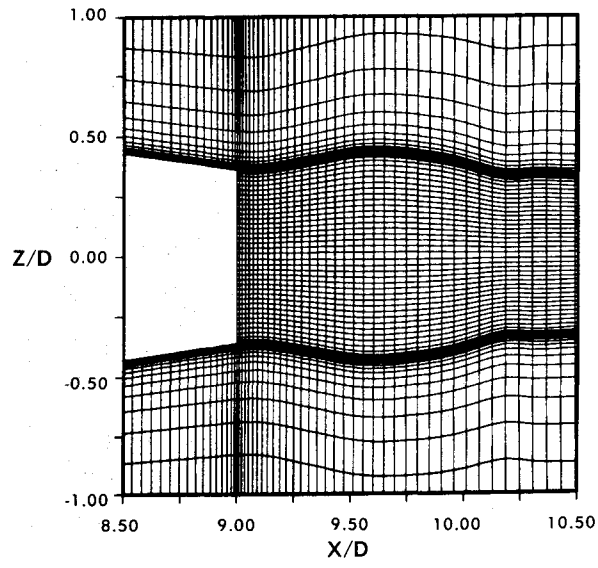

Fig. 4 Computational grid in the base region, jet on, $P_j/P_\infty = 3.0$.

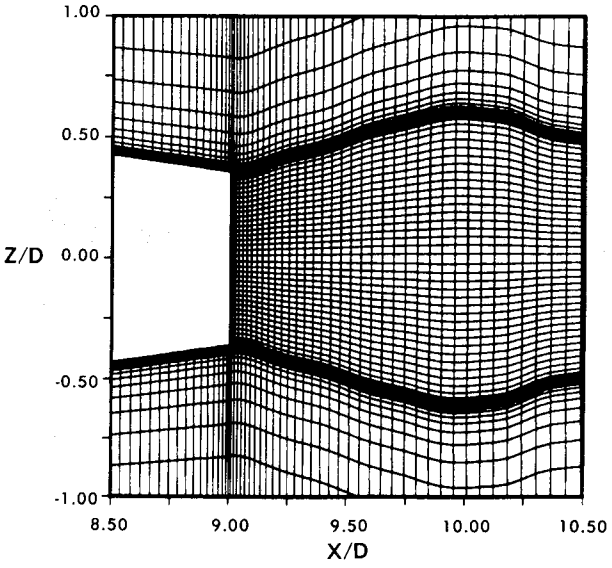

Fig. 5 Computational grid in the base region, jet on, $P_j/P_\infty = 9.0$.

Results

All the computations were made at $M_\infty = 2.0$, $\alpha = 0$, and for a jet exit Mach number of 2.5. Solutions were obtained for the jet-off and jet-on cases for jet-to-freestream pressure ratios of $P_j/P_\infty = 1$, 3, and 9. Figure 6 shows a schematic illustration of the base flow for the jet-on condition and its associated nomenclature.

Figure 7 shows the velocity vectors in the base region for the jet-off case. The recirculatory flow in the near wake is clearly evident. The expected velocity defect can also be seen further downstream in this figure. The effect of the centered propulsive jet on the base region flowfield is shown in Figs. 8-10 for $P_j/P_\infty = 1$, 3, and 9, respectively. Figure 8a shows the velocity vectors in the near wake for a pressure ratio of 1. The flowfield in the base region has changed considerably and the large recirculatory bubble seen for the jet-off condition is much reduced. This small separation bubble is a region of counterclockwise recirculating flow and can be seen near the base corner as shown in Fig. 8b. Similar features can be seen for the pressure ratio $P_j/P_\infty = 3$, as

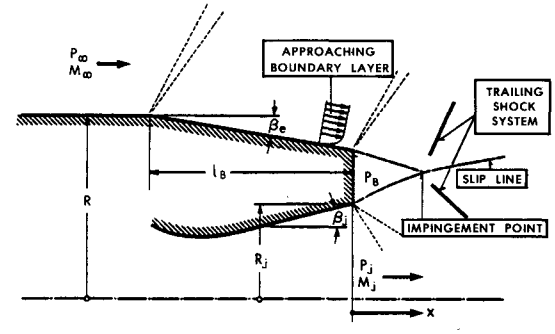

Fig. 6 Schematics of the afterbody flow with jet.

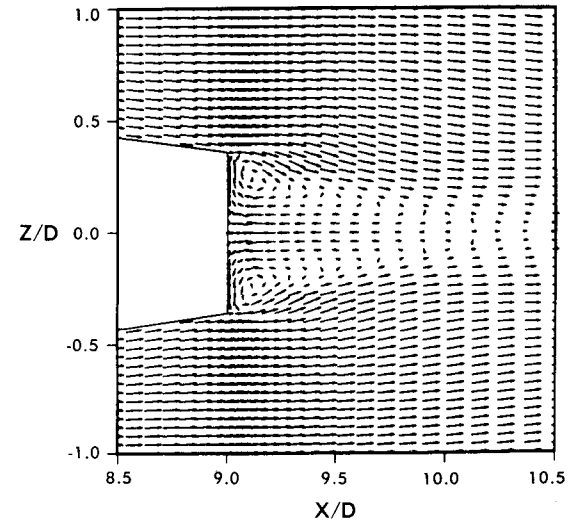

Fig. 7 Velocity vectors in the base region, $M_\infty = 2.0$, jet off.

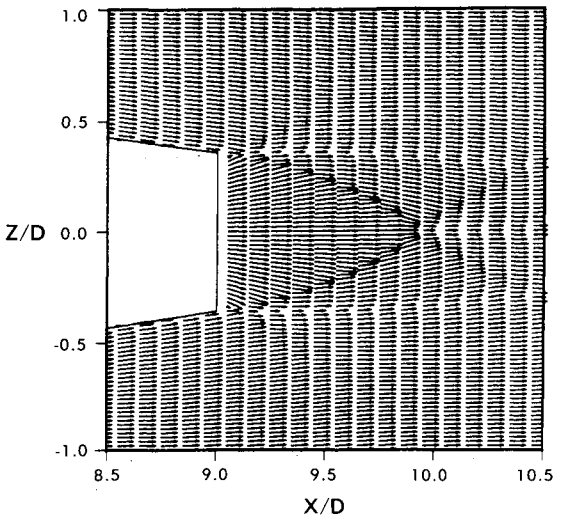

Fig. 8a Velocity vectors in the base region, $M_\infty = 2.0$, $M_j = 2.5$, $P_j/P_\infty = 1.0$, jet on.

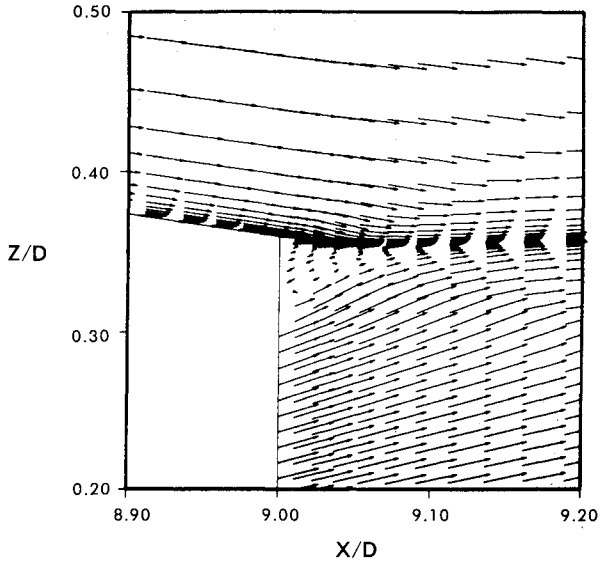

Fig. 8b Velocity vectors expanded near the base corner, $M_\infty = 2.0$, $M_j = 2.5$, $P_j/P_\infty = 1.0$, jet on.

shown in Fig. 9. In both Figs. 8 and 9, one can observe the oblique compression shock wave at the end of the afterbody and the barrel shock inside the plume indicated by the turning of the velocity vectors. As seen in Fig. 9, the previous numerical result[5] does not show the shock structure observed experimentally in the base region in terms of the computed contours; the dark lines were drawn by hand to emphasize its resemblance to the experiment. In contrast, our present results show the computed density contours that come directly from the flowfield solutions and clearly show the shock structure in the base region. This is the first time such a striking comparison of the computed base region flowfield with the associated shock structure in the experiment has been shown for these flows and all details of the flowfield are captured rather well. Figure 10a shows the velocity city vectors for the high pressure ratio case of $P_j/P_\infty = 9$. The shape of the plume is clearly shown. An expanded view of the flowfield near the end of the afterbody and the base corner is shown in Fig. 10b. This figure shows an extensive region of flow separation upstream of the base corner. The

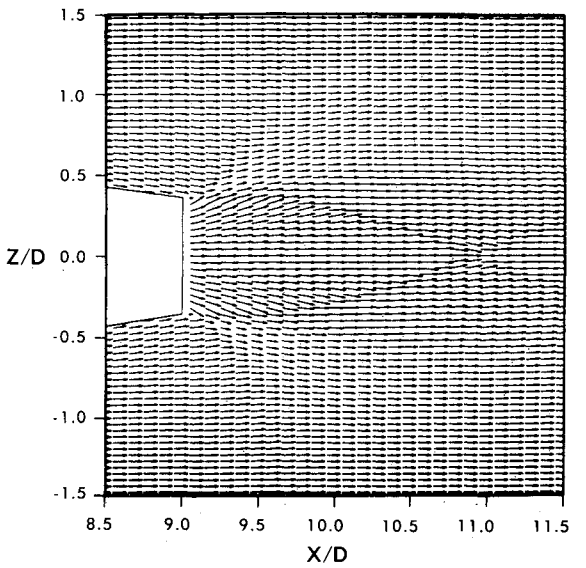

Fig. 9 Velocity vectors in the base region, $M_\infty = 2.0$, $M_j = 2.5$, $P_j/P_\infty = 3.0$, jet on.

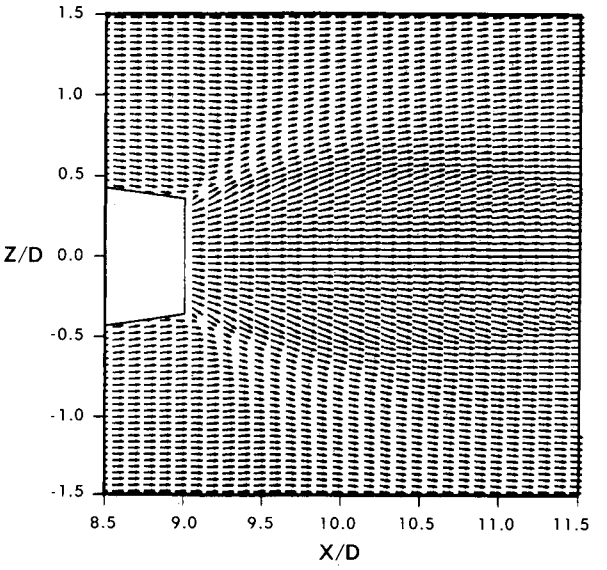

Fig. 10a Velocity vectors in the base region, $M_\infty = 2.0$, $M_j = 2.5$, $P_j/P_\infty = 9.0$, jet on.

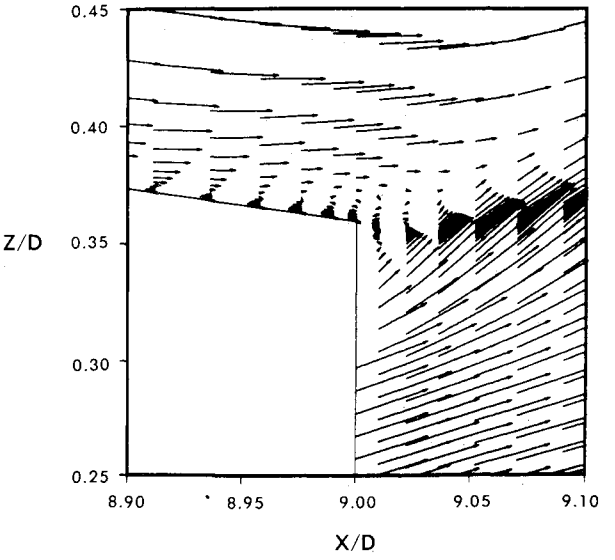

Fig. 10b Velocity vectors expanded near the base corner, $M_\infty = 2.0$, $M_j = 2.5$, $P_j/P_\infty = 9.0$, jet on.

small separation bubble seen downstream of the base corner for the lower pressure ratio case is virtually eliminated. The separation bubble upstream of the base corner is confined to the boundary layer on the afterbody. Additionally, the compression shock wave seen at the end of the afterbody with the lower jet pressure has now moved further upstream of the base corner with the high jet exit pressure.

Figures 11–14 show the comparisons of the computed density contours and the experimental schlieren pictures[9] for the jet-off and jet-on cases with $P_j/P_\infty = 1$, 3, and 9, respectively. These schlieren photographs are for the same geometry and flow conditions obtained from the experimental study of Agrell and While.[14] Figure 11 shows the comparison for the jet-off condition. For this case, the expansions at the base corner, the free shear layer, and the recompression shock downstream of the base are all clearly observed in the computed results and agree very well with the experimental observations. Comparisons for the jet-on conditions are shown in Figs. 12–14 and it is clear that flow features in the base region have changed due to the presence of the jet. Figure 12 shows the results for the jet pressure ratio of 1. The flow features to be seen are the oblique shock at the end of the afterbody, the trailing shock system inside the plume, and the slip line that emanates from the nozzle lip and defines the jet boundary. The trailing shock inside the plume closes about one-half caliber downstream of the exit plane and results in a Mach reflection. As the jet-to-freestream pressure ratio is increased to 3.0, the trailing shocks inside the plume cross each other about 2 calibers downstream of the base (see Fig. 13). Other features are similar to the pressure ratio equals one case. Details of the flow features in the base region are changed as the jet exit pressure ratio is increased to 9. The trailing shock system seen with the lower pressure ratios is not observed in either the computation or experiment (see Fig. 14). For this higher jet pressure ratio, one can observe a lambda shock near the base corner, which induces a separation region on the afterbody just upstream of the base corner. The agreement between the computed and the experimentally observed flow features is very good for both jet-off and jet-on conditions.

Quantitatively, one is interested in how the complex flowfield in the base region affects the base pressure. Figure 15 shows the base pressure as a function of boattail angles for the jet-off condition. Although experimental measurements were made for various boattail angles, computations were restricted to only the 8 deg case. The computed base pressure agrees well with the experimental data. The centered jet affects the base region flowfield considerably and, thus, has a strong affect on the base pressure. The effect of the jet on the base pressure for various jet-to-freestream pressure ratios is shown in Fig. 16. The trend of an increase in base pressure with jet pressure seen experimentally is clearly predicted by the numerical solutions. In addition, the present results are in better agreement with experiment than the previous results from Ref. 5. Good agreement is found at the high pressure ratio with the present result. Some disagreement, however, is observed at the lower pressure ratios. The present results were obtained using a CDC 7600 computer. A typical case took about 3.5 h of CPU to obtain the converged result.

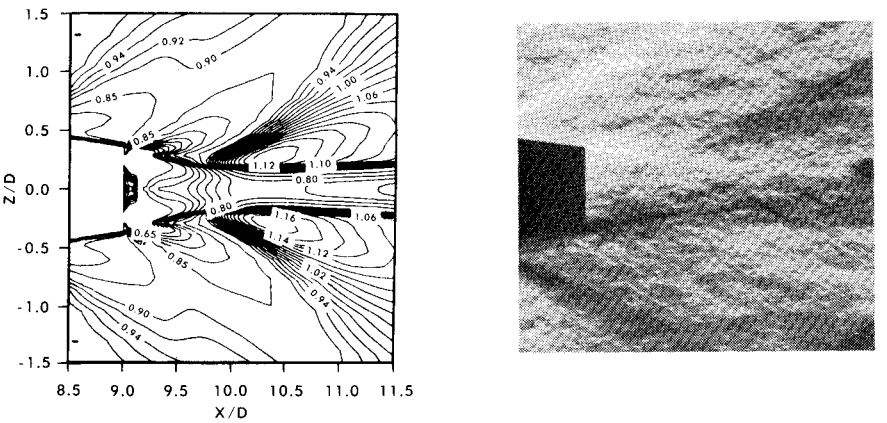

Fig. 11 Computed density contours; experimental schlieren photograph, $M_\infty = 2.0$, jet off.

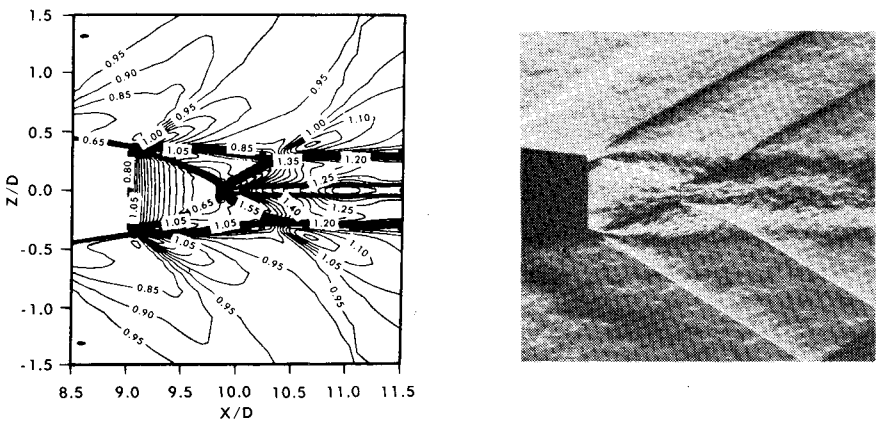

Fig. 12 Computed density contours; experimental schlieren photograph, $M_\infty = 2.0$, $M_j = 2.5$, $P_j/P_\infty = 1.0$, jet on.

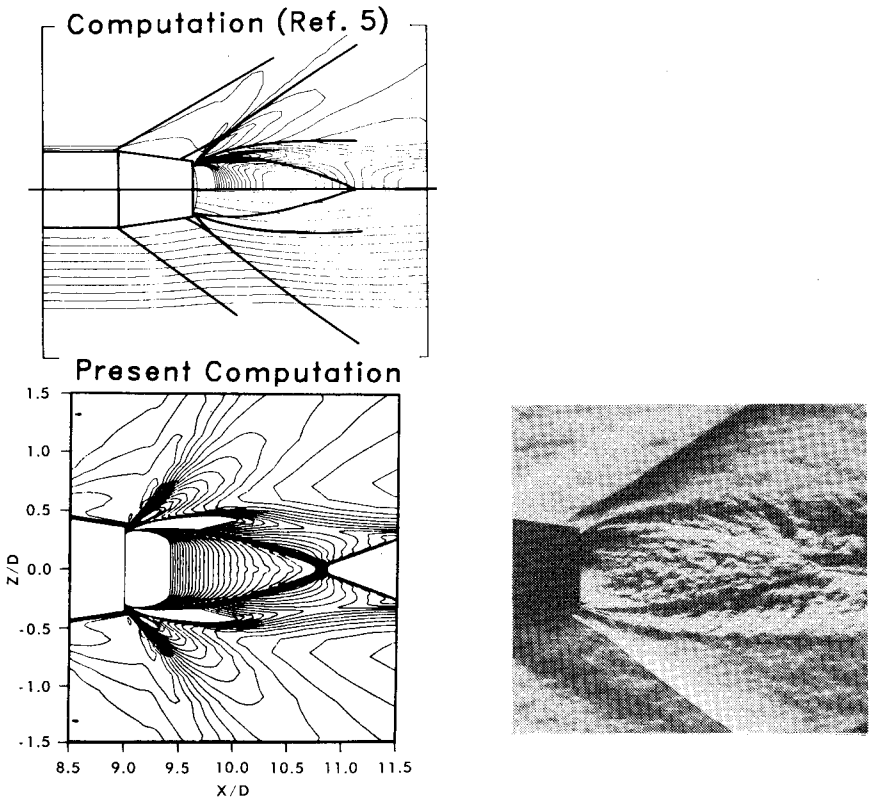

Fig. 13 Computed density contours; experimental schlieren photograph, $M_\infty = 2.0$, $M_j = 2.5$, $P_j/P_\infty = 3.0$, jet on.

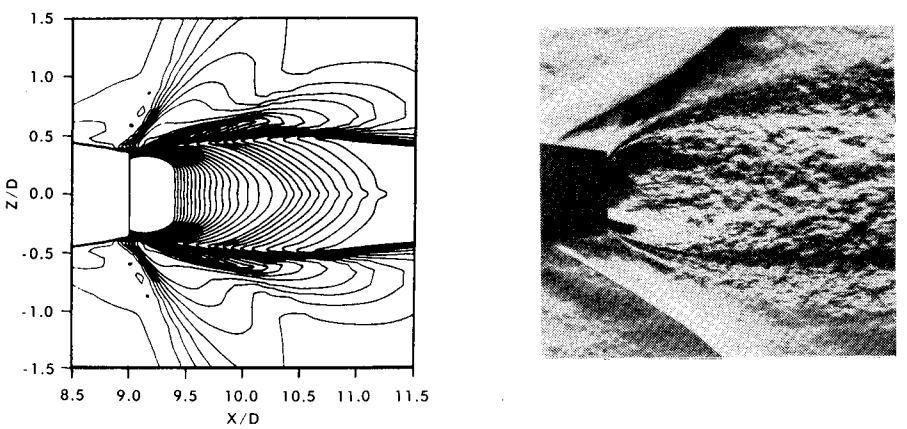

Fig. 14 Computed density contours; experimental schlieren photograph, $M_\infty = 2.0$, $M_j = 2.5$, $P_j/P_\infty = 9.0$, jet on.

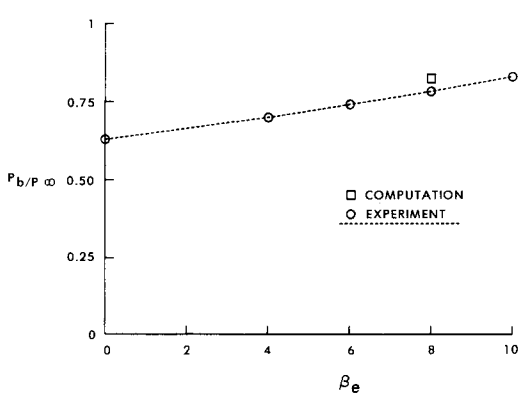

Fig. 15 Variation of base pressure with boattail angle, $M_\infty = 2.0$, jet off.

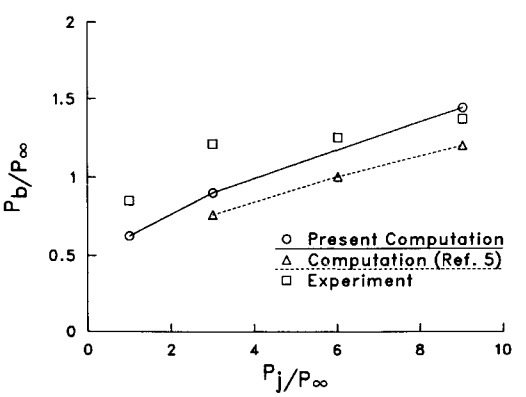

Fig. 16 Variation of base pressure with jet pressure, $M_\infty = 2.0$, jet on.

Conclusions

A computational study was made for supersonic flow over a missile afterbody in the presence of a centered propulsive jet using a time-dependent, thin-layer Navier-Stokes code. Qualitative features of the base region flowfield such as the compression shock, plume shape, and trailing shock system seen experimentally were easily observed in the computed results. Quantitative comparisons indicate good agreement for the jet-off case. Also, the predicted effect of the jet on the base pressure has the correct trend observed experimentally. Some disagreement at lower pressure ratios exists. The accuracy of these predictions should improve for finer computational grids and as turbulence modeling used for these flows improves.

References

[1]Korst, H.H., "A Theory for Base Pressures in Transonic and Supersonic Flow," *Journal of Applied Mechanics,* Dec. 1956, pp. 593-600.

[2]Chow, W.L., "The Effect of Boattailing of a Projectile in Transonic Flow," *Proceedings of Third Symposium on Numerical and Physical Aspects of Aerodynamic Flows,* Long Beach, CA, June 1985, pp. 338-395.

[3]Sahu, J., Nietubicz, C.J., and Steger, J.L., "Numerical Computation of Base Flow for a Projectile at Transonic Speeds," U.S. Army Ballistic Research Laboratory, Aberdeen Proving Ground, MD, ARBRL-TR-02495, June 1983 (AD A130293); see also AIAA Paper 82-1358, Aug. 1982.

[4]Sahu, J. and Nietubicz, C.J., "Numerical Computation of Base Flow for a Missile in the Presence of a Centered Jet," U.S. Army Ballistic Research Laboratory, Aberdeen Proving Ground, MD, ARBRL-MR-3397, U.S. Army, Oct. 1984 (AD A148784); see also AIAA Paper 84-0527, Jan. 1984.

[5]Deiwert, G.S., "Supersonic Axisymmetric Flow Over Boattails Containing a Centered Propulsive Jet," *AIAA Journal,* Vol. 22, Oct. 1984, pp. 1358-1365.

[6]Fox, J.H., "Predicting Plume-Induced Separation on Bluff-Base Bodies," AIAA Paper 84-0315, Jan. 1984.

[7]Wagner, B., "Calculation of Turbulent Flow About Missile Afterbodies Containing an Exhaust Jet," AIAA Paper 84-1659, June 1984.

[8]Thomas, P.D., Reklis, R.P., Roloff, R.R., and Conti, R.J., "Numerical Simulation of Axisymmetric Base Flow on Tactical Missiles with Propulsive Jet," AIAA Paper 84-1658, June 1984.

[9]Baldwin, B.S. and Lomax, H., "Thin-Layer Approximation and Algebraic Model for Separated Turbulent Flows," AIAA Paper 78-257, 1978.

[10]Nietubicz, C.J., Pulliam, T.H., and Steger, J.L., "Numerical Solution of the Azimuthal-Invariant Thin-Layer Navier-Stokes Equations," U.S. Army Ballistic Research Laboratory, Aberdeen Proving Ground, MD, ARBRL-TR-02227, March 1980 (AD A085716).

[11]Steger, J.L., "Implicit Finite-Difference Simulation of Flow About Arbitrary Geometries with Application to Airfoils," *AIAA Journal,* Vol. 16, July 1978, pp. 679-686.

[12]Pulliam, T.H. and Steger, J.L., "On Implicit Finite-Difference Simulations of Three-Dimensional Flow," *AIAA Journal,* Vol. 18, Feb. 1980, pp. 159-167.

[13]Beam, R. and Warming, R.F., "An Implicit Factored Scheme for the Compressible Navier-Stokes Equations," AIAA Paper 77-645, June 1977.

[14]Agrell, J. and White, R.A., "An Experimental Investigation of Supersonic Axisymmetric Flow Over Boattails Containing a Centered Propulsive Jet," FFA Technical Note AU-913, 1974.